Journal of Colloid and Interface Science 622 (2022) 539–548

Contents lists available at ScienceDirect

Journal of Colloid and Interface Science

journal homepage: www.elsevier.com/locate/jcis

Embedding indium nitride at the interface of indium-oxide/indium-zinc-sulfide heterostructure with enhanced interfacial charge transfer for high photocatalytic hydrogen evolution

Huihui Zhang, Huajun Gu, Xiaohao Wang, Lingfeng Li, Juhua Zhang, Shengyuan Chang, Wei-Lin Dai *

Department of Chemistry and Shanghai Key Laboratory of Molecular Catalysis and Innovative Materials, Fudan University, Shanghai 200433, PR China

GRAPHICAL ABSTRACT

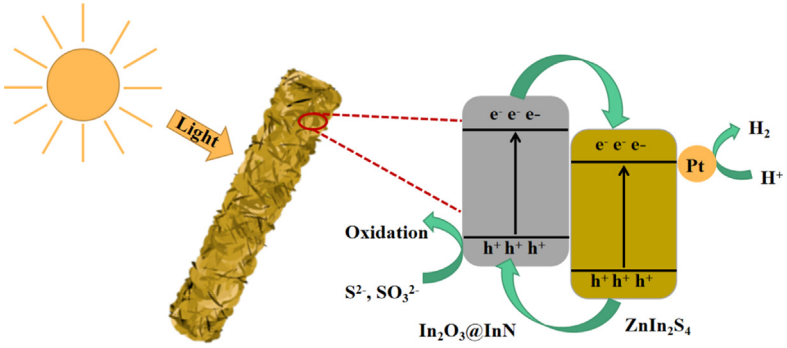

ARTICLE INFO

Article history:
Received 4 March 2022
Revised 19 April 2022
Accepted 21 April 2022
Available online 27 April 2022

Keywords:
Indium nitride
Indium-oxide/indium-zinc-sulfide
Heterostructure
Interfacial charge transfer
Photocatalytic hydrogen evolution

ABSTRACT

Enhancing the interfacial charge carriers transfer efficiency is important for designing photocatalysts with excellent hydrogen evolution performance. In this work, we have successfully constructed a In_2O_3@InN/$ZnIn_2S_4$ ternary heterostructure by embedding InN at the interface of thin-layered $ZnIn_2S_4$ and tubular In_2O_3 derived from metal-organic frameworks (MOFs) nanorods for the first time. The InN can not only adjust the energy band structure of In_2O_3, but also boost the photogenerated charge carriers transfer at the interface of In_2O_3 and $ZnIn_2S_4$. The optimum photocatalytic hydrogen evolution rate of In_2O_3@InN/$ZnIn_2S_4$ composite reaches 275 μmol/h (50 mg of catalyst) under simulated sunlight irradiation, which is obviously higher than pure In_2O_3 (12.5 times), $ZnIn_2S_4$ (2.5 times) and binary In_2O_3/$ZnIn_2S_4$ (1.8 times) photocatalysts. This work can offer a meaningful strategy to promote the interfacial charge separation in the heterostructure for excellent photocatalytic hydrogen evolution activity.

1. Introduction

Nowadays, the energy crisis and environmental pollution have become two social concerns due to the extensive use of fossil fuels [1]. Hydrogen is considered as an ideal alternative energy source, which has special properties, such as high calorific value, carbon-free attributes and so on [2]. Since Fujishima and Honda firstly reported the electrochemical photolysis of water at a titanium dioxide electrode in 1972 [3], the exploration of excellent catalysts for photocatalytic hydrogen evolution via water-splitting has become a research hotspot in the field of renewable energy conversion [4–9]. In the past few years, a great number of highly efficient photocatalysts have been reported, such as g-C_3N_4 [10,11], metal oxides

* Corresponding author.
E-mail address: wldai@fudan.edu.cn (W.-L. Dai).

https://doi.org/10.1016/j.jcis.2022.04.118
0021-9797/

[12,13], metal sulfides [14–16], metal nitrides [17,18] and metal-organic-frameworks (MOFs) [19–23]. However, the catalytic performance of single catalyst is largely limited due to its poor light absorption capacity and rapid recombination of the photogenerated charge carriers. Therefore, constructing heterostructure systems is an effective strategy for higher photocatalytic activity [24–27].

$ZnIn_2S_4$, which has a narrow band gap and a suitable conduction band potential for proton reduction, has been regarded as an ideal photocatalyst [17,28–31]. However, its photocatalytic performance is deeply restricted by the rapid recombination of the photogenerated charge carriers. In recent years, materials derived from MOFs have been used as photocatalysts for water splitting [32–36], which show a lot of special properties. Among them, In_2O_3 is a well-known semiconductor derived from In-MOF, which can combine with other nanomaterials as an excellent carrier [37–43]. Various photocatalysts based on MOF-derived In_2O_3 have been synthesized, such as In_2O_3/Bi_2O_3 [37], $In_2O_3/g\text{-}C_3N_4$ [38,39], In_2O_3/CdS [40], In_2O_3/CuO [41], In_2O_3/SnO_2 [42], $In_2O_3/CdZnS$ [43] and $In_2O_3/ZnIn_2S_4$ [44]. However, the detailed photocatalytic mechanism of the composites is still unclear and need to be further studied.

It is known that InN has high electron density and an excellent electron transport property [45], besides, its visible light absorption is much higher than many other semiconductors with a narrow band gap of around 0.7 eV [46]. Thus, a number of InN-based photocatalysts have been reported, including InN/TiO_2 [46], InN/ZnO [47] and InN/GaZnON [48]. However, the construction and the photocatalytic hydrogen evolution performance of In_2O_3/InN composite have not been reported up to now.

In particular, a MOF-derived $In_2O_3/ZnIn_2S_4$ heterostructure has been reported in our group previously [44], in which the In-N-In sites can boost the interfacial charge transfer for enhanced photocatalytic hydrogen evolution. However, the detailed effect mechanism of In-N-In sites is still needed to be investigated (pure InN phase cannot be determined, at least in the TEM images). Therefore, in this work, we further explored the effect of crystalline InN phase in the heterostructural composite and a novel ternary photocatalyst In_2O_3@InN/$ZnIn_2S_4$ was synthesized by facile hydrothermal and calcination methods for the first time. Under sunlight irradiation, the optimum hydrogen evolution rate reaches a value of 275 μmol/h, when the mass ratio of In_2O_3 and melamine is set at 1: 20, about 12.5, 2.5 and 1.8 times higher than the pure In_2O_3, $ZnIn_2S_4$ and $In_2O_3/ZnIn_2S_4$, respectively. The enhanced photocatalytic activity can be attributed to the formation of heterostructure with InN embedded at the interface of In_2O_3/$ZnIn_2S_4$ heterostructure, further accelerating the migration of the interfacial photogenerated charge carriers. Furthermore, this work can provide some new strategies for boosting the interfacial charge carriers transfer in heterostructure composite.

2. Materials and methods

2.1. Materials

2-Aminoterephthalic acid (99%) and zinc chloride ($ZnCl_2$, 98%) were purchased from Aldrich. Indium chloride tetrahydrate ($InCl_3 \cdot 4H_2O$, 99.9%) was purchased from Aladdin, and other chemicals of analytical grade were purchased from Sinopharm Chemical Reagent Co. Ltd. All reagents were used without further purification.

2.2. Preparation of samples

2.2.1. Preparation of In-MOF

The synthesis of In-MOF nanorods refers to our previous work [44]. In detail, 598 mg of $In(NO_3)_3 \cdot 4.5H_2O$ and 234 mg of 2-aminoterephthalic acid are added into 20 mL of *N,N*-dimethylformamide (DMF) and stirred for 30 min. Then, the dispersion is transferred into a 50 mL Teflon-lined autoclave and kept at 125 ℃ for 5 h. After natural cooling to room temperature, the product is collected by centrifuging and washing with DMF and ethanol for several times, respectively. Finally, the In-MOF sample is obtained after drying overnight at 80 ℃.

2.2.2. Preparation of In_2O_3

The above In-MOF precursors are put into a crucible and covered with an aluminum foil. Then, the samples are calcined at 500 ℃ for 2 h in N_2 atmosphere to get the pure In_2O_3.

2.2.3. Preparation of In_2O_3@InN

The melamine is used as the source of nitrogen element, and the In_2O_3@InN composites with different InN ratios are firstly synthesized through a facile calcination method. In detail, 50 mg of the above In_2O_3 and a certain amount of melamine are mixed in a mortar. After absolute grinding, the mixture is put into a crucible and covered with an aluminum foil. Followed with calcination at 700 ℃ for 4 h under N_2 atmosphere, the obtained sample is labeled as In_2O_3@InN. Different mass ratio of the In_2O_3 to InN (1:2, 1:5, 1:20, 1:40, 1:60) are prepared by adding different amounts of melamine (0.1 g, 0.25 g, 1.0 g, 2.0 g, 3.0 g). For comparison, 650 and 750 ℃ are also used as calcination temperature.

2.2.4. Preparation of In_2O_3@InN/$ZnIn_2S_4$

The ternary catalysts with different amount of $ZnIn_2S_4$ are synthesized by a typical hydrothermal method [44]. In detail, 18 mg of In_2O_3@InN is added into 10 mL of the mixed solution of water and glycerol (v: v = 4: 1), followed with ultrasound treatment for 30 min. Afterwards, 163 mg of $ZnCl_2$, 351 mg of $InCl_3 \cdot 4H_2O$ and 180 mg of thioacetamide (TAA) are added into the above dispersion and stirred for 30 min. Then, the mixture is placed and heated in a water bath at 80 ℃ for 90 min under continuous stirring. After natural cooling, the samples can be collected by centrifuging and washing with deionized water and ethanol for several times, and the products are labeled as In_2O_3@InN/$ZnIn_2S_4$ after drying at 80 ℃ overnight. For comparison, different mass ratio of In_2O_3@InN to $ZnIn_2S_4$ (1:1, 1:2, 1:4) are synthesized by adjusting the amount of In_2O_3@InN, and the pure $ZnIn_2S_4$ is prepared by a similar process without adding In_2O_3@InN.

2.2.5. Preparation of comparative samples

$In_2O_3/ZnIn_2S_4$ is prepared by adding MOF-derived In_2O_3 instead of In_2O_3@InN. The catalyst synthesized by directly mixing In_2O_3@InN and the $ZnIn_2S_4$ is labeled as M-sample.

2.3. Characterization

The crystal structures of the samples are measured by X-ray diffraction (XRD) (D2, Bruker Corp., Germany). The morphologies and microstructure of the composites are observed with scanning electron microscopy (SEM, Phenom Prox, Netherlands) and field-emission transmission electron microscopy (FE-TEM, Tecnai G2 F20 STwin, FEI). The specific surface area (S_{BET}) and pore size distribution are tested via N_2 absorption–desorption isotherms, which are performed at liquid nitrogen temperature (77 K) on Micromeritics Tristar 3020 and ASAP 2020 Plus apparatus. The surface element composition and valence state of the photocatalysts are analyzed by X-ray photoelectron spectroscopy (XPS, PHI 5300) with contaminant carbon (C 1s = 284.6 eV) as a reference to calibrate the binding energies. The optical properties of the samples are recorded using an ultraviolet–visible diffuse reflectance spectrometer (Lambda 650S, PERKIN ELMER) equipped with an integration sphere and $BaSO_4$ as reference. The photoluminescence

(PL) spectra are obtained with a fluorescence spectrophotometer (Agilent, Cary Eclipse) at the emission wavelength of 420 nm.

2.4. Photocatalytic hydrogen evolution tests

The photocatalytic hydrogen evolution tests are examined in a closed system with a gas recirculation. The light source is a 300 W Xe lamp (CEL-HXF-300), and the temperature is controlled at 20 ℃ by cooling circulating water. In detail, 50 mg of photocatalyst is added into 100 mL of deionized water containing Na_2SO_3 (0.25 M) and $Na_2S{\cdot}9H_2O$ (0.35 M) as sacrificial agents. Then, 1% Pt is added to the system as co-catalyst. Afterwards, the mixture is poured into the reactor and evacuated by a vacuum pump. The hydrogen evolution amount is determined by a gas chromatograph fitted with a 5 Å molecular sieve column and a thermal conductivity detector (TCD). Apparent quantum efficiency (AQE) is measured using different monochromatic light filter (320, 350, 400, 420, 450 nm) and is calculated according to the following equation:

$$\mathrm{AQE}\,(\%) = \frac{\text{number of reacted electrons}}{\text{number of incident photons}} \times 100\%$$

$$= \frac{\text{number of evolved } H_2 \text{ molecules} \times 2}{\text{number of incident photons}} \times 100\%$$

2.5. Photoelectrochemical tests

The photoelectrochemical measurements are carried out on an electrochemical workstation (Chenhua CHI760E, China) with a standard three-electrode system. The working electrodes are prepared as follows: 2 mg of photocatalyst powder is dispersed in a mixed solution containing 400 μL of water, 45 μL of ethanol and 5 μL of Nafion. Followed with ultrasound treatment for 30 min, the 100 μL of resultant suspension is dropped and dried on a FTO substrate (1×1 cm^2). After being dried at room temperature, the FTO glass is used as the working electrode, and a Pt foil and a saturated calomel electrode (SCE) are used as the counter electrode and reference electrode, respectively. The photocurrent curves and Mott-Schottky curves are measured in a Na_2SO_4 (0.5 M) aqueous solution, where a 300 W Xe lamp is used as light source. Electrochemical impedance spectroscopy (EIS) plots are detected in a mixed solution of potassium ferricyanide (0.025 M) and muriate of potash (0.1 M).

2.6. Computation method

The Vienna Ab Initio Package (VASP) [49,50] is employed to perform all the density functional theory (DFT) calculations within the generalized gradient approximation (GGA) using the PBE [51] formulation. The projected augmented wave (PAW) potentials [52,53] have been used to describe the ionic cores and take valence electrons into account using a plane wave basis set with a kinetic energy cutoff of 450 eV. Partial occupancies of the Kohn-Sham orbitals are allowed using the Gaussian smearing method and a width of 0.05 eV. It is considered that electronic energy is self-consistent when the energy change is smaller than 10^{-4} eV and the geometry optimization is considered convergent when the force change is smaller than 0.03 eV/Å. Grimme's DFT-D3 methodology [54] is used to describe the dispersion interactions. The Brillouin zone integral uses the surfaces structures of $2 \times 2 \times 1$ monkhorst pack K-point sampling. In particular, the adsorption energies (E_{ads}) are calculated as $E_{ads} = E_{ad/sub} - E_{ad} - E_{sub}$, and the $E_{ad/sub}$, E_{ad} and E_{sub} are the optimized adsorbate/substrate system, the adsorbate in the structure and the clean substrate respectively. The free energies are obtained by formula $G = E_{total} + E_{ZPE} - TS$, and the E_{total}, E_{ZPE}, and TS are the ground-state energy, zero-point energies, and entropy terms, respectively, with the latter two taking vibration frequencies from DFT.

3. Results and discussion

3.1. Morphology and structure characterization

The synthesis process of In_2O_3@InN/$ZnIn_2S_4$ can be illustrated in Fig. 1. Firstly, the In-MOF nanorods are synthesized by a typical method as described previously. Next, the tubular In_2O_3 is obtained by calcining In-MOF nanorods at 500 ℃ in N_2 atmosphere, and the X-ray diffraction (XRD) patterns of the as-synthesized In_2O_3 is displayed in Fig. S1. The diffraction peaks coincide well with the cubic In_2O_3 (JCPDS: 060416). Afterwards, the calcination reactions are employed to synthesize In_2O_3@InN nanotubes with In_2O_3 and melamine as precursors. Finally, In_2O_3@InN/$ZnIn_2S_4$ heterostructure is formed via a facile hydrothermal method.

The morphology and microstructure of the composites are observed by scanning electron microscope (SEM) and field-emission transmission electron microscopy (FE-TEM) analyses. The SEM images display the In-MOF nanorods and In_2O_3 nanotubes, and the latter are synthesized by In-MOF pyrolysis (Fig. 2a and b). Compared to the In-MOF precursor, the tubular In_2O_3 is slightly curved, and its diameter is smaller, mainly due to the inhomogeneous shrinkage of microcrystalline during the pyrolysis process [44]. As Fig. 2c shows, after calcination reaction, the In_2O_3@InN composite maintains the tubular structure with a shorter length, implying the structure of the main catalyst is stable in the synthesis processes.

The FE-TEM images further demonstrate the tubular structure of In_2O_3@InN composite (Fig. 3a and b). Meanwhile, the interface of the composite can be clearly seen in Fig. 3c. The lattice distance of 0.29 and 0.207 nm can be assigned to the (222) crystal plane of In_2O_3 and (102) crystal plane of InN, further confirming the successful conversion of In_2O_3 to InN crystal. Besides, the elemental mappings of the In_2O_3@InN imply that all elements are evenly distributed in the composite (Fig. 3d–i) and the atomic ratio is shown in Fig. S2. It should be noted that the N element is from the organic ligands of MOF and the added melamine. In addition, the irregular structure of the pristine $ZnIn_2S_4$ can be observed in Fig. S3.

As Fig. 4a–c shows, the FE-TEM images and enlarged TEM images of In_2O_3@InN/$ZnIn_2S_4$ further corroborate that the layered $ZnIn_2S_4$ is loaded on the surface of tubular In_2O_3@InN after the hydrothermal process. The co-existence of In_2O_3, InN and $ZnIn_2S_4$ can be clearly observed in Fig. 4d, which is circled with number 1, 2 and 3. The lattice distance of 0.29, 0.207 and 0.32 nm can be attributed to the (222) crystal plane of In_2O_3, (102) crystal plane of InN and (222) crystal plane of $ZnIn_2S_4$, respectively, indicating the successful synthesis of In_2O_3@InN/$ZnIn_2S_4$ ternary heterostructure. Additionally, as Fig. S4 shows, the elemental mappings of the ternary heterostructure further confirm the even distribution of thin-layered $ZnIn_2S_4$ on In_2O_3@InN nanotubes.

Fig. 5a shows the XRD patterns of the In_2O_3@InN with different mass of melamine as precursors. As for the pure In_2O_3, the main diffraction peaks of 21.5°, 30.6°, 35.5°, 51.0° and 60.7° are corresponded to the diffraction planes (211), (222), (400), (440) and (622) of cubic In_2O_3. Compared to pure In_2O_3, a new diffraction peak of 33.2° appears after the calcination process obviously, which is assigned to the (101) crystal planes of hexagonal InN [46], confirming the partial conversion of In_2O_3 to InN and the successful synthesis of In_2O_3@InN. The reaction mechanism can be explained as follows. The ammonia gas from the decomposition of the melamine is firstly absorbed on the surface of In_2O_3 nanotubes, then, the surficial In_2O_3 can react with ammonia to form

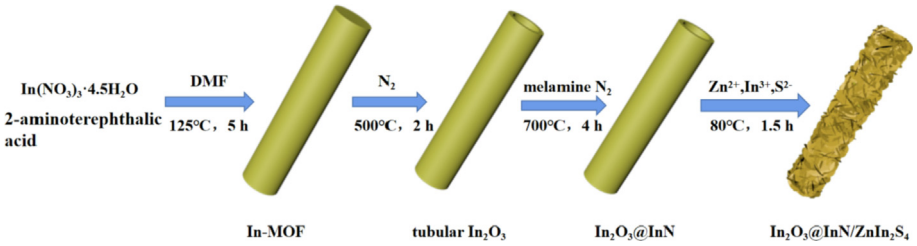

Fig. 1. Schematic illustration of the preparation of In_2O_3@InN/$ZnIn_2S_4$.

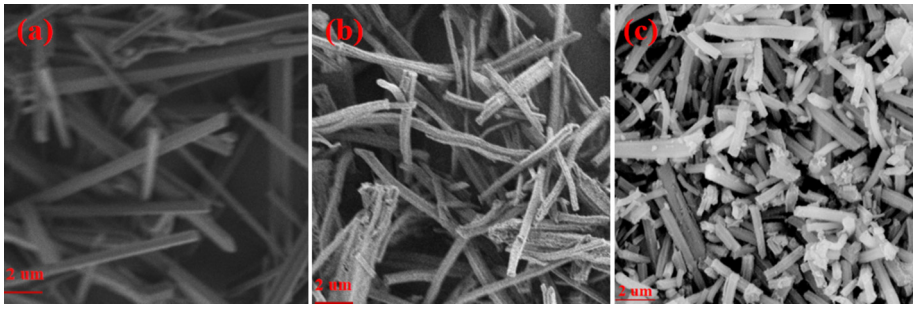

Fig. 2. SEM images of (a) In-MOF, (b) In_2O_3 and (c) In_2O_3@InN.

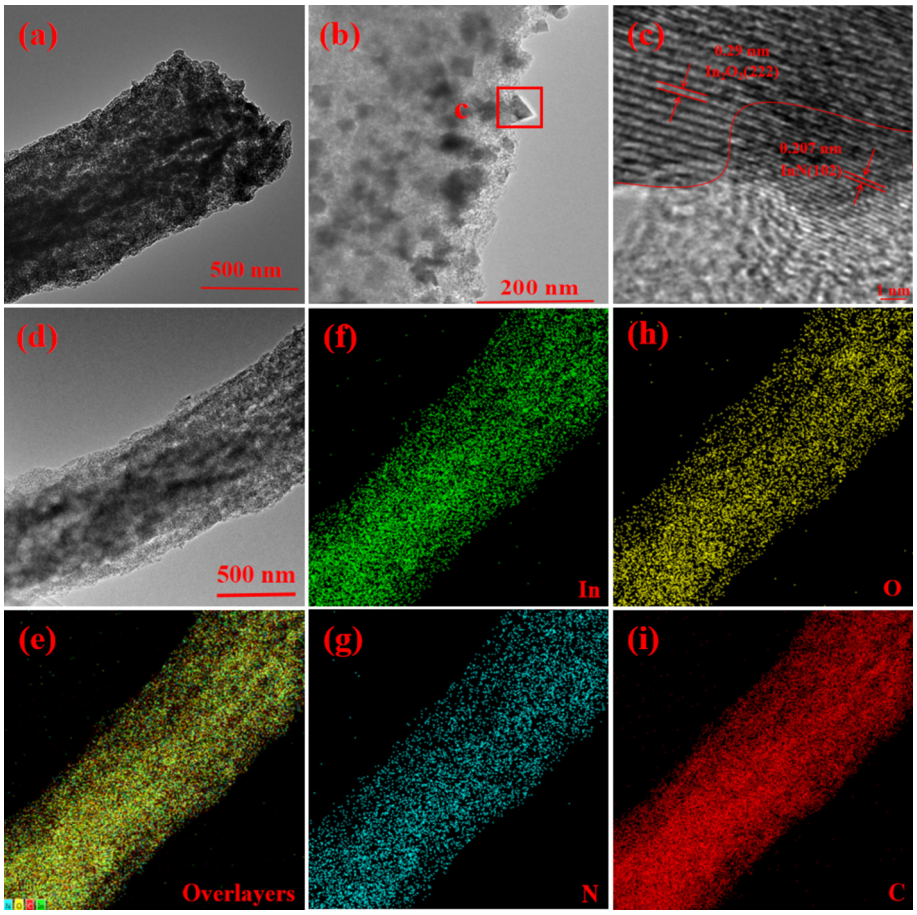

Fig. 3. (a and b) FE-TEM, (c) HRTEM images, (d–i) elemental mapping profiles of In_2O_3@InN.

InN at 700 ℃ [46]. Meanwhile, with the increasing amount of melamine added, the peak intensity of InN enhances, implying more In_2O_3 is converted to InN. As Fig. S5 shows, the calcination temperature also influences the mass ratio of InN in the composites. From the XRD patterns showed in Fig. 5b, it can be seen that the diffraction peaks of 21.6°, 27.7°, 47.2°, 52.6° and 55.6° are corresponded

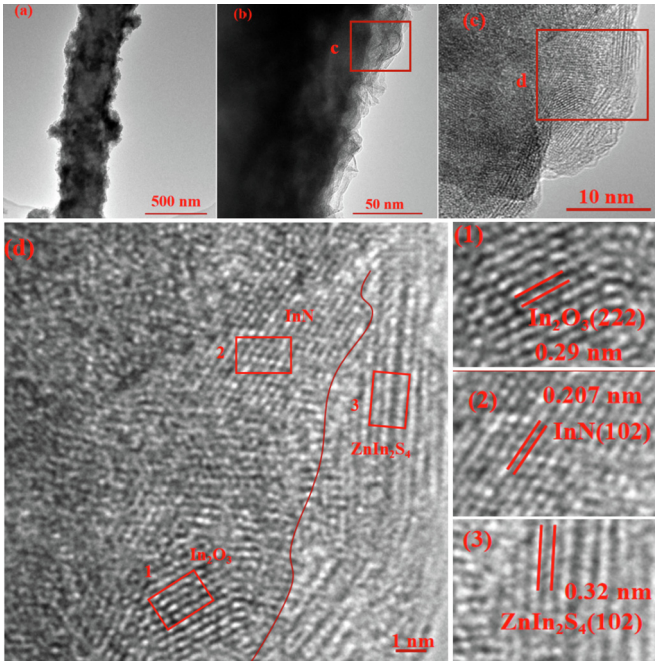

Fig. 4. (a b) FE-TEM and (c d) HRTEM images of In_2O_3@InN/$ZnIn_2S_4$, the marked 1, 2, 3 represent the In_2O_3, InN and $ZnIn_2S_4$.

to the diffraction planes (006), (102), (110), (116), (022) of hexagonal $ZnIn_2S_4$, suggesting the successful synthesis of the heterostructure. However, compared with In_2O_3@InN, the diffraction peak intensity of InN at 33.2° in the ternary heterostructure is not obvious (Fig. S6), as a result of the tiny amount and low diffraction intensity of InN.

The specific surface area (S_{BET}) and pore size distribution of samples can be estimated by N_2 absorption–desorption isotherms. As depicted in Fig. 6a, compared to pristine In_2O_3 (76 m^2/g), the S_{BET} of In_2O_3@InN (84 m^2/g) is slightly increased, which is mainly attributed to the gas-involved calcination process. As depicted in Fig. 6b, the pristine $ZnIn_2S_4$ has a relatively low S_{BET} of 20.1 m^2/g. After coupling with In_2O_3@InN nanotubes, the ternary composite shows a significantly higher S_{BET} of 158.1 m^2/g, confirming the thin-layered $ZnIn_2S_4$ is well distributed on the In_2O_3@InN nanotubes. This result implies the ternary photocatalyst with a high S_{BET} could offer more active sites for water splitting. And the pore size distributions of samples are displayed in Fig. S7.

The Raman spectroscopy can analyze the carbon constituent of the photocatalysts. As displayed in Fig. 7a, In_2O_3 displays two prominent D and G bands, indicting the existence of partly graphitized carbon [55–57], which is formed in the pyrolysis process of In-MOF. At the same time, the binary and ternary photocatalysts display the two bands, demonstrating the partly graphitized carbon is stable in the calcination and hydrothermal processes, mainly because all the calcination processes are performed at an inert atmosphere. In addition, compared with In_2O_3, the I_D/I_G value of In_2O_3@InN is obviously increased, indicating the formation of defects upon the high temperature calcination process of In_2O_3.

The optical properties of the photocatalysts can be analyzed via UV–Vis. diffuse reflectance spectroscopy (UV–Vis. DRS), and the results shown in Fig. 7b demonstrate that the In_2O_3 has intense response in a wide light range, while the visible light absorption intensity of $ZnIn_2S_4$ is weak with an absorption edge at around 520 nm. Moreover, the band gap energy of $ZnIn_2S_4$ is evaluated to be 2.25 eV by the Kubelka-Munk method (Fig. S8). Compared with In_2O_3/$ZnIn_2S_4$, the absorption edge wavelengths of the ternary photocatalyst decreases obviously, implying the light absorption capacity is not the decisive factor for the enhanced photocatalytic hydrogen evolution activity in this work. Furthermore, the visible light absorption intensity of the ternary photocatalysts is enhanced with the increasing mass ratio of InN, as shown in Fig. S9, and the calcination temperature also influences the optical properties of the ternary materials.

The surface chemical composition and chemical states of elements are investigated by X-ray photoelectron spectroscopy (XPS). Fig. S10 reveals the existence of C, O, N, Zn, In, S elements in the photocatalysts. As Fig. 8a shows, the binding energies at 444.6 and 455.2 eV are assigned to the In-O bond in In_2O_3 and In_2O_3@InN. In addition, the appeared two peaks at 443.5 and 451.2 eV can be ascribed to the In-N bond in In_2O_3@InN. At the same time, the N 1s spectra of the In_2O_3 can be divided into two peaks at 398.8 and 400.8 eV, assigned to the lattice N and N—C bond. Furthermore, the new peak at 397.1 eV is belonged to N-In bond in In_2O_3@InN (Fig. 8b). Therefore, the results further confirm the formation of InN crystal in the calcination process. The binding energies located at 1021.5 and 1044.5 eV can be assigned to the Zn^{2+} in the $ZnIn_2S_4$ (Fig. S11a). Moreover, the S 2p spectrum can be divided into two peaks at 161.9 and 162.9 eV (Fig. S11c), which are attributed to S^{2-} in the $ZnIn_2S_4$. Meanwhile, after coupling with $ZnIn_2S_4$ layer, unapparent binding energy shifts of Zn 2p, S 2p, In 3d can be observed (Fig. S11), revealing the surface chemical composition of the as-obtained photocatalysts is stable. It should be noted that the peaks for In 3d in In_2O_3/$ZnIn_2S_4$ and ternary composites are consistent with the $ZnIn_2S_4$, mainly because the $ZnIn_2S_4$ is located on the surface of In_2O_3 or In_2O_3@InN nanotubes in the composites.

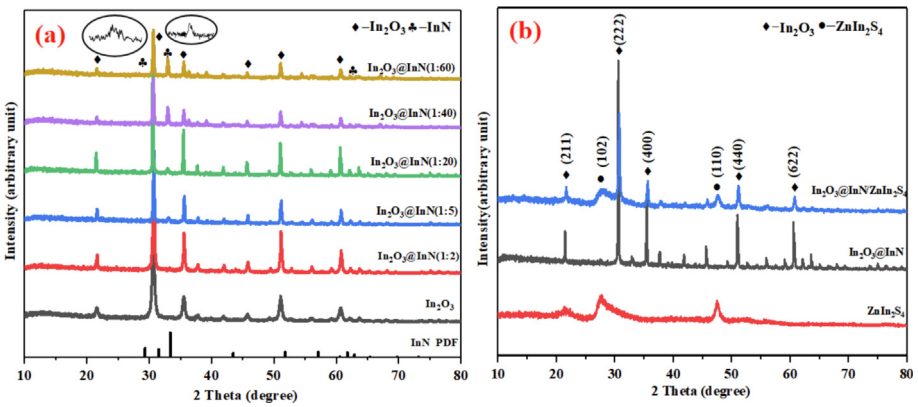

Fig. 5. (a and b) XRD patterns of various catalysts.

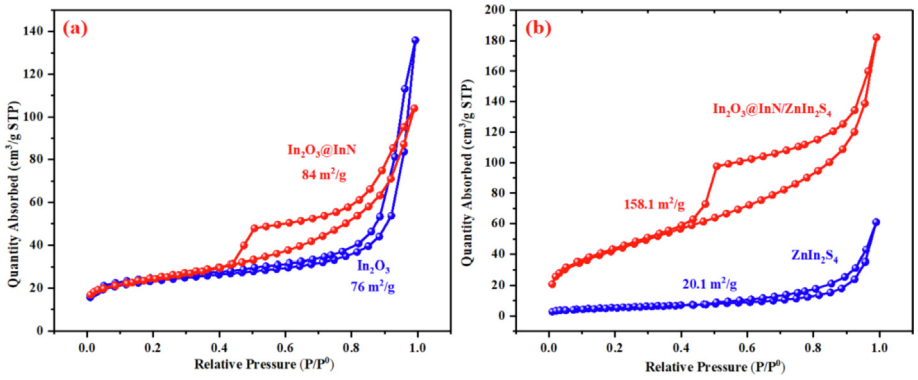

Fig. 6. N_2 absorption–desorption isotherms of In_2O_3 and In_2O_3@InN (a), $ZnIn_2S_4$ and In_2O_3@InN/$ZnIn_2S_4$ (b).

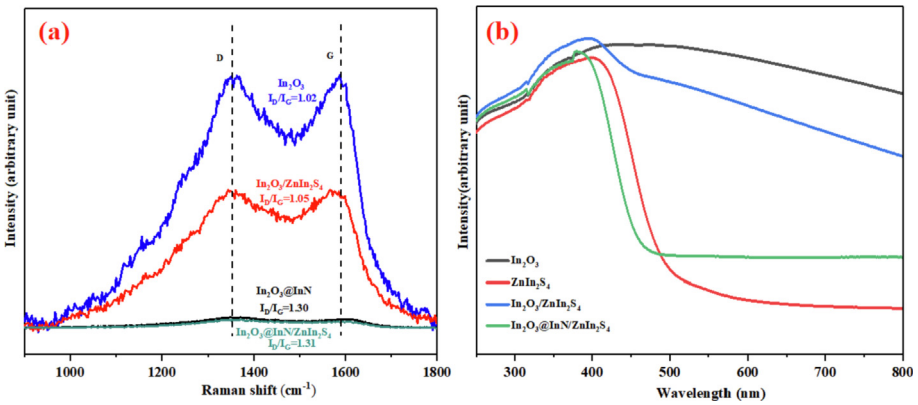

Fig. 7. (a) Raman spectra, (b) UV–Vis. DRS spectra of various catalysts.

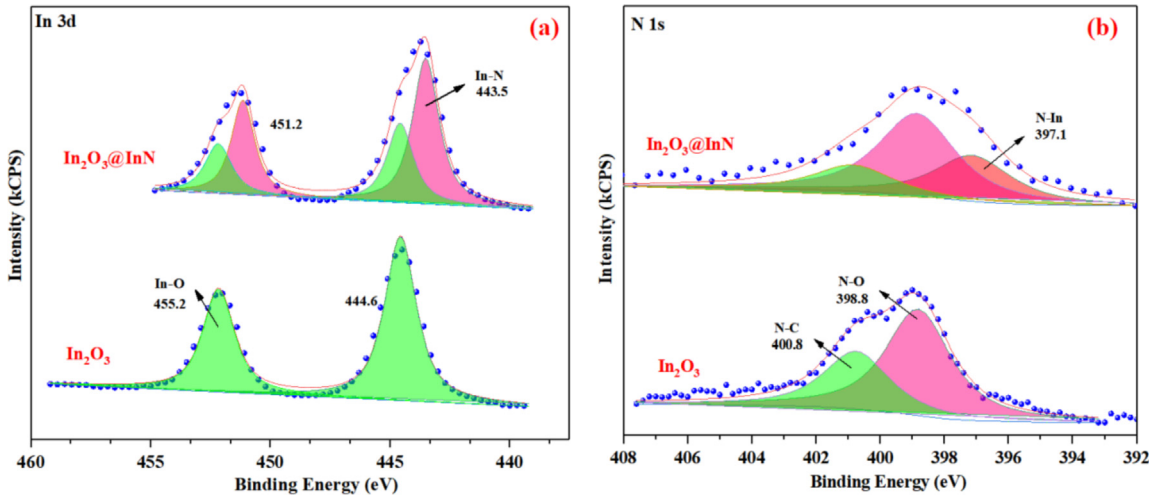

Fig. 8. (a) In 3d, (b) N 1s XPS spectra of In_2O_3 and In_2O_3@InN.

3.2. Photocatalytic activity test

The photocatalytic performance of the as-prepared samples can be tested with photocatalytic hydrogen evolution, using Na_2SO_3 and $Na_2S{\cdot}9H_2O$ as scavengers under simulated sunlight irradiation. All hydrogen evolution activities are tested by four parallel experiments. Firstly, as Fig. 9a–c shows, by adjusting the mass ratio of In_2O_3 and melamine precursors, as well as the temperature of the calcination, the In_2O_3@InN has the highest hydrogen evolution rate when the mass ratio of the added In_2O_3 and melamine precursors is 1: 20 and the calcination temperature is at 700 ℃. Then, the amount of $ZnIn_2S_4$ loaded is further optimized (Fig. S12). Overall, according to the relationship of hydrogen evolution performance and the mass of catalysts (Fig. S13a), the ternary composite In_2O_3@InN/$ZnIn_2S_4$ reaches the optimum hydrogen evolution rate of 275 μmol/h (50 mg of catalyst), which is about 12.5 and 2.5 times folder than the pristine In_2O_3 (22 μmol/h) and $ZnIn_2S_4$ (112 μmol/h), respectively. It is worthy to note that the highest rate is 1.8 times than the binary composite In_2O_3/$ZnIn_2S_4$, suggesting the InN plays an important role in enhancing the photocatalytic hydro-

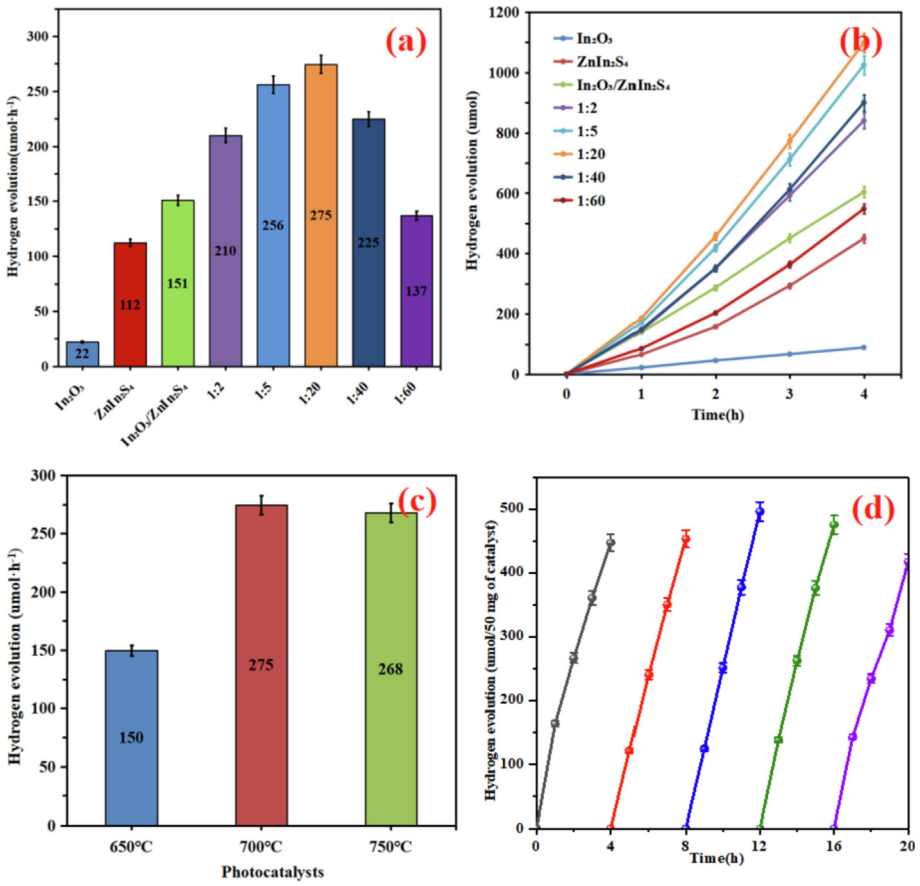

Fig. 9. (a–c) H_2 evolution rate of comparative samples, (d) recycling H_2 evolution over In2O3@InN/ZnIn2S4 in four repeated tests.

gen evolution activity. At the same time, the hydrogen evolution rate of the ternary composite prepared by hydrothermal method is obviously higher than the sample prepared by mechanical mixing the In_2O_3@InN and $ZnIn_2S_4$ (Fig. S14), demonstrating the importance of core–shell structure for hydrogen evolution. In addition, the optimum ternary In_2O_3@InN/$ZnIn_2S_4$ photocatalyst has a superior hydrogen evolution activity among MOF-derived In_2O_3-based photocatalysts ever reported as Table S1 shows. For comparison, the hydrogen evolution activities of the optimal In_2O_3@InN/$ZnIn_2S_4$ photocatalyst in other sacrificial systems (methanol and lactic acid) are also tested. As shown in Fig. S15, the hydrogen evolution rates are obviously lower than that in Na_2S-Na_2SO_3 mixture, mainly because the photocatalytic system is more suitable for the weak alkaline environment [44]. The apparent quantum efficiencies (AQE) are further investigated under the same reaction conditions using specific incident wavelengths, and the AQE of In_2O_3@InN/$ZnIn_2S_4$ is calculated as about 2.96% at 350 nm (Fig. S13b). In addition, the stability is a vital property of photocatalysts. As illustrated in Fig. 9d, the hydrogen evolution rate is almost constant with the initial rate after five successive cycles. Moreover, the XRD pattern of the ternary composite after five cycles is nearly unchanged compared with the fresh photocatalyst, further indicating its excellent photocatalytic stability (Fig. S16).

3.3. Investigation of charge transfer efficiency

The photogenerated charges transfer efficiency is a vital factor affecting the hydrogen evolution performance of the photocatalysts. To further investigate the transfer and recombination behaviors of the photogenerated charges in the ternary composite, photocurrent responses, electrochemical impedance spectra (EIS) and photoluminescence (PL) spectroscopy are performed. As illustrated in Fig. 10a, the PL emission intensity of In_2O_3/$ZnIn_2S_4$ is slightly weaker than the pristine $ZnIn_2S_4$, due to the reduced recombination of charge carriers. After embedding InN at the interface of In_2O_3/$ZnIn_2S_4$ heterostructure, the PL intensity decreases sharply, implying the InN can further accelerate the interfacial charge transfer between In_2O_3 and $ZnIn_2S_4$. As shown in Fig. 10b, the photocurrent response of the In_2O_3@InN/$ZnIn_2S_4$ ternary composite is significantly higher than the pristine materials and the binary samples, indicating the enhanced separation and transfer efficiency of photogenerated charges. Meanwhile, the EIS spectra shows the ternary photocatalyst has the smallest semicircle Nyquist plots (Fig. 10c), which demonstrates the In_2O_3@InN/$ZnIn_2S_4$ has the optimal charges transfer performance compared to other counterparts, and this finding is consistent with PL and photocurrent responses results.

3.4. Theoretical calculation and possible photocatalytic mechanism

Furthermore, as depicted in Fig. S17, the flat bands of In_2O_3, In_2O_3@InN and $ZnIn_2S_4$ are estimated using Mott-Schottky plots, which are −0.69, −0.98 and −0.43 eV (vs SCE), respectively. As the electric potential of NHE is about 0.22 eV higher than SCE and the potential of the conduction band (CB) is 0.2 eV lower than flat band potential, the accurate CB of In_2O_3, In_2O_3@InN and $ZnIn_2S_4$ are predicted to be −0.67, −0.96 and −0.41 eV (vs NHE). It should be noted that the CB of In_2O_3@InN is about 0.3 eV lower than the pristine In_2O_3. As shown in Fig. S18, the valence band (VB) of materials can be analyzed by VB XPS spectrum, and the VB potential of In_2O_3 is estimated as 1.81 eV according to the formula: $E_{NHE} = \Phi + 1.80–4.44$ (E_{NHE}: potential vs NHE; Φ: 4.5 eV, the electron work function of the analyzer) [58]. It is found that the VB potential of In_2O_3@InN is about 1.48 eV, obviously lower than that

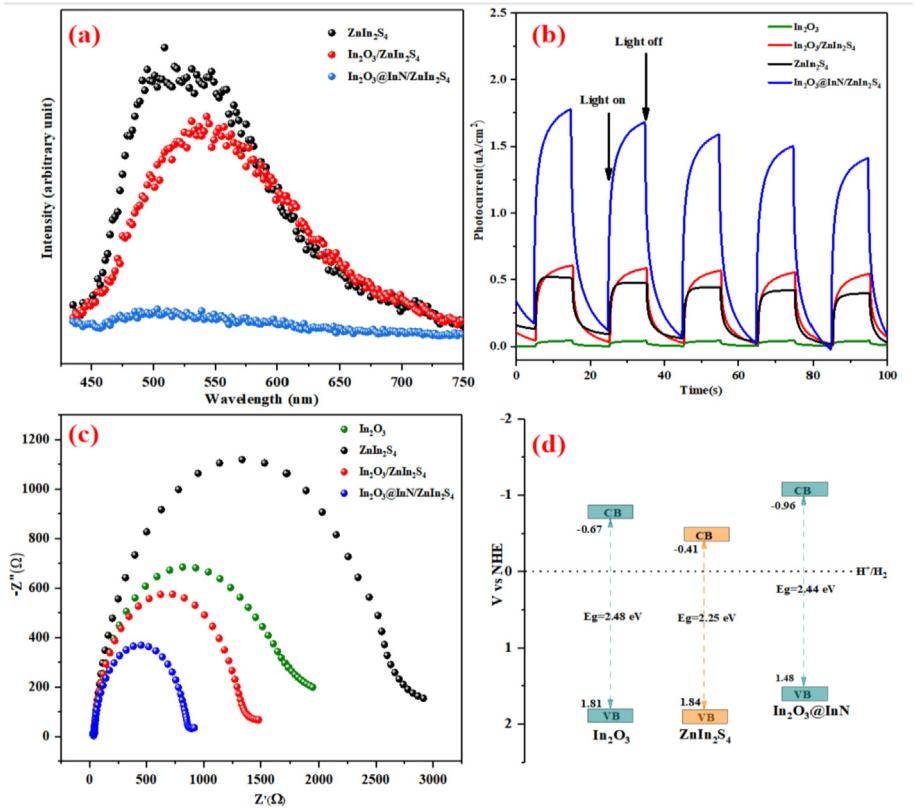

Fig. 10. (a) PL spectra (excited at 420 nm), (b) EIS Nyquist plots, (c) transient photocurrent of the as-obtained photocatalysts, (d) schematic illustration of band positions for In_2O_3, In_2O_3@InN and $ZnIn_2S_4$.

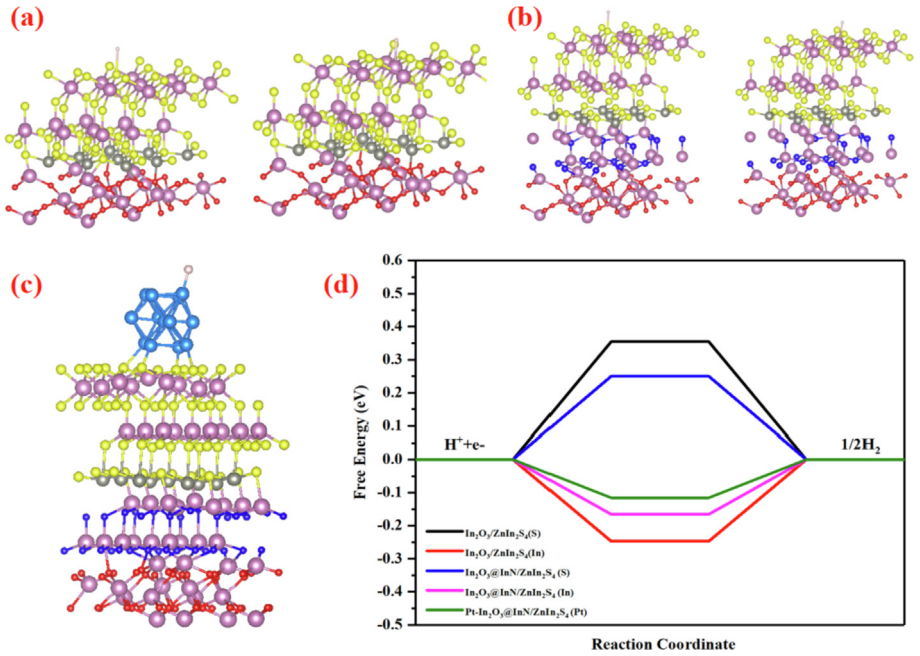

Fig. 11. Schematic structure models of H adsorption site of (a) S atom (left) and In atom (right) on $In_2O_3/ZnIn_2S_4$, (a) S atom (left) and In atom (right) on In_2O_3@InN/$ZnIn_2S_4$, (c) Pt atom on Pt-In_2O_3@InN/$ZnIn_2S_4$. The red, purple, navy blue, gray, yellow, blue and pink balls are O, In, N, Zn, S, Pt and H atoms, respectively. (d) Free energy diagrams of reaction coordinates on photocatalysts. (For interpretation of the references to colour in this figure legend, the reader is referred to the web version of this article.)

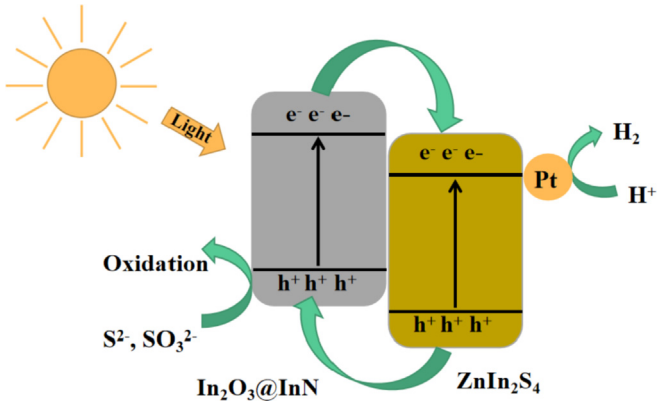

Fig. 12. Illustration of the proposed charges transfer mechanism of In_2O_3@InN/$ZnIn_2S_4$ heterostructure.

of In_2O_3. At the same time, the VB potential of $ZnIn_2S_4$ can be estimated as 1.48 eV with its CB potential and band gap energy, and the latter is obtained by the Kubelka-Munk method. As a consequence, the band structures of pristine samples can be illustrated in Fig. 10d.

In order to further explore the mechanism of the enhanced photocatalytic performance, a theoretical calculation is conducted based on density functional theory (DFT). As Fig. 11a–c shows, several possible schematic structure models of H absorption sites on photocatalysts are constructed. And the Gibbs free energy of these sites are calculated. Based on the previous report, the Gibbs free energy of an excellent photocatalyst should be close to zero. As depicted in Fig. 11d, compared with S atom and In atom site, the Gibbs free energy of Pt atom site on Pt-In_2O_3@InN/$ZnIn_2S_4$ is obviously closer to zero, which implies a smaller energy barrier for the photocatalytic hydrogen evolution reaction. On the other hand, this result confirms that the ternary photocatalyst system with Pt as co-catalyst has the lowest overpotential for the reaction, and the best photocatalytic hydrogen evolution performance.

Based on the above discussions, a possible photocatalytic hydrogen evolution mechanism can be proposed (Fig. 12). In the hierarchical structure, the excited carriers migrate from In_2O_3@InN to $ZnIn_2S_4$ under the simulated sunlight irradiation, leading to reduced recombination of charge carriers. In particular, InN can adjust the surface composition and the band structure of In_2O_3, resulting in acceleration of the interfacial charges transfer between In_2O_3 and $ZnIn_2S_4$, so as to greatly boost the photocatalytic performance.

4. Conclusion

In summary, we have successfully synthesized a novel In_2O_3@InN/$ZnIn_2S_4$ ternary heterostructure by facile calcination and hydrothermal methods for the first time. The optimal ternary photocatalyst exhibits a superior hydrogen evolution rate of 275 μmol/h (50 mg of catalyst) under simulated sunlight irradiation, which is so far an especially high value among several representative MOF-derived In_2O_3-based photocatalysts for hydrogen evolution reported previously [38,40,43]. Various characterization technologies and DFT calculation have confirmed the fabrication and the superior photocatalytic performance of the ternary composite. In particular, the embedded InN not only adjusts the energy band of In_2O_3, but also accelerates the charge transfer at the interface of In_2O_3/$ZnIn_2S_4$ heterostructure, which can explain the superior performance of the ternary photocatalyst to the binary In_2O_3/$ZnIn_2S_4$ composite reported recently [44]. This work might provide a novel strategy to boost the interfacial charge transfer in the heterostructure for enhanced photocatalytic hydrogen evolution performance. Further study on the exploration of the embedded InN in other kinds of composite photocatalysts are being underway.

CRediT authorship contribution statement

Huihui Zhang: Conceptualization, Methodology, Investigation, Validation, Writing – original draft. **Huajun Gu:** Writing – review & editing. **Xiaohao Wang:** Validation. **Lingfeng Li:** Formal analysis. **Juhua Zhang:** Formal analysis. **Shengyuan Chang:** Validation. **Wei-Lin Dai:** Funding acquisition, Project administration, Supervision, Writing – review & editing, Visualization.

Declaration of Competing Interest

The authors declare that they have no known competing financial interests or personal relationships that could have appeared to influence the work reported in this paper.

Acknowledgements

This work was financially supported by Natural Science Foundation of Shanghai (19ZR1403500), National Natural Science Foundation of China (NNSFC, Project 21373054), and Natural Science Foundation of Shanghai Science and Technology Committee (19DZ2270100).

Appendix A. Supplementary material

Supplementary data to this article can be found online at https://doi.org/10.1016/j.jcis.2022.04.118.

References

[1] J.D. Chen, Q.L. Xie, M. Shahbaz, M.L. Song, Y.L. Wu, The fossil energy trade relations among BRICS countries, Energy 217 (2021) 119383.
[2] S.E. Hosseini, M.A. Wahid, Hydrogen production from renewable and sustainable energy resources: Promising green energy carrier for clean development, Renew. Sust. Energ. Rev. 57 (2016) 850–866.
[3] AKIRA Fujishima, KENICHI Honda, Electrochemical photolysis of water at a semiconductor electrode, Nature 238 (5358) (1972) 37–38.
[4] W. Hu, L. Lin, R. Zhang, C. Yang, J. Yang, Highly efficient photocatalytic water splitting over edge-modified phosphorene nanoribbons, J. Am. Chem. Soc. 139 (43) (2017) 15429–15436.
[5] S. Chen, G. Ma, Q. Wang, S. Sun, T. Hisatomi, T. Higashi, Z. Wang, M. Nakabayashi, N. Shibata, Z. Pan, T. Hayashi, T. Minegishi, T. Takata, K. Domen, Metal selenide photocatalysts for visible-light driven Z-scheme pure water splitting, J. Mater. Chem. A. 7 (13) (2019) 7415–7422.
[6] W. Wang, M. Xu, X. Xu, W. Zhou, Z. Shao, Perovskite oxide based electrodes for high-performance photoelectrochemical water splitting, Angew. Chem. Int. Ed. 59 (1) (2020) 136–152.
[7] T. Hisatomi, J. Kubota, K. Domen, Recent advances in semiconductors for photocatalytic and photoelectrochemical water splitting, Chem. Soc. Rev. 43 (22) (2014) 7520–7535.
[8] S.Y. Tee, K.Y. Win, W.S. Teo, L.D. Koh, S.H. Liu, C.P. Teng, M.Y. Han, Recent progress in energy-driven water splitting, Adv. Sci. 4 (2017) 1600337.
[9] B.G. Ng, L.K. Putri, X.Y. Kong, Y.W. Teh, P. Pasbakhsh, S.P. Chai, Z-scheme photocatalytic systems for solar water splitting, Adv. Sci. 7 (2020) 1903171.
[10] H.J. Dong, Y. Zuo, N. Song, S.H. Hong, M.Y. Xiao, D.Q. Zhu, J.X. Sun, G. Chen, C.M. Li, Bimetallic synergetic regulating effect on electronic structure in cobalt/vanadium co-doped carbon nitride for boosting photocatalytic performance, Appl. Catal., B. 287 (2021) 119954.
[11] C.C. Han, P.F. Su, B.H. Tan, X.G. Ma, H. Lv, C.Y. Huang, P. Wang, Z.F. Tong, G. Li, Y. Z. Huang, Z.F. Liu, Defective ultra-thin two-dimensional g-C_3N_4 photocatalyst for enhanced photocatalytic H_2 evolution activity, J. Colloid Interface Sci. 581 (2021) 159–166.
[12] J. Zhang, Z. Yu, Z. Gao, H. Ge, S. Zhao, C. Chen, S. Chen, X. Tong, M. Wang, Z. Zheng, Y. Qin, Porous TiO_2 nanotubes with spatially separated platinum and CoO_x cocatalysts produced by atomic layer deposition for photocatalytic hydrogen production, Angew. Chem. Int. Ed. 56 (3) (2017) 816–820.
[13] J.Q. Pan, Z.J. Dong, B.B. Wang, Z.Y. Jiang, C. Zhao, J.J. Wang, C.S. Song, Y.Y. Zheng, C.R. Li, The enhancement of photocatalytic hydrogen production via Ti^{3+} self-doping black TiO_2/g-C_3N_4 hollow core-shell nano-heterojunction, Appl. Catal., B. 242 (2019) 92–99.

[14] C. Ding, C. Zhao, S. Cheng, X. Yang, Ultrahigh photocatalytic hydrogen evolution performance of coupled 1D CdS/1T-phase dominated 2D WS_2 nanoheterojunctions, Chin. J. Catal. 43 (2) (2022) 403–409.
[15] X.H. Wang, L.F. Li, H.J. Gu, H.H. Zhang, J.H. Zhang, Q. Zhang, W.L. Dai, Highly efficient noble-metal-free NiS/rGO/$Cd_{0.3}Zn_{0.7}S$ nanorods in visible-light-driven H_2 evolution with enhanced surface photoinduced charge transfer, Appl. Surf. Sci. 574 (2022) 151553.
[16] K. Zhang, L.J. Guo, Metal sulfide semiconductors for photocatalytic hydrogen production, Catal Sci. Technol. 3 (2013) 1672–1690.
[17] S.Q. Gong, Z.J. Jiang, P.H. Shi, J.C. Fan, Q.J. Xu, Y.L. Min, Noble-metal-free heterostructure for efficient hydrogen evolution in visible region: molybdenum nitride/ultrathin graphitic carbon nitride, Appl. Catal., B. 238 (2018) 318–327.
[18] M.G. Kibria, F.A. Chowdhury, S. Zhao, B. Alotaibi, M.L. Trudeau, H. Guo, Z. Mi, Visible light-driven efficient overall water splitting using p-type metal-nitride nanowire arrays, Nat. Com. 6 (2015) 6797.
[19] Y. Su, Z. Zhang, H. Liu, Y. Wang, $Cd_{0.2}Zn_{0.8}S$@UiO-66-NH_2 nanocomposites as efficient and stable visible-light-driven photocatalyst for H_2 evolution and CO_2 reduction, Appl. Catal., B. 200 (2017) 448–457.
[20] H.-L. Tang, X.-J. Sun, F.-M. Zhang, Development of MOF-based heterostructures for photocatalytic hydrogen evolution, Dalton Trans. 49 (35) (2020) 12136–12144.
[21] Q. Zhang, H.J. Gu, X.H. Wang, L.F. Li, J.H. Zhang, H.H. Zhang, Y.F. Li, W.L. Dai, Robust hollow tubular $ZnIn_2S_4$ modified with embedded metal-organic-framework-layers: extraordinarily high photocatalytic hydrogen evolution activity under simulated and real sunlight irradiation, Appl. Catal., B. 298 (2021) 120632.
[22] B.J. Zhu, R.Q. Zou, Q. Xu, Metal-organic framework based catalysts for hydrogen evolution, Adv. Energy Mater. 8 (2018) 1801193.
[23] J.-D. Xiao, Q. Shang, Y. Xiong, Q. Zhang, Y.i. Luo, S.-H. Yu, H.-L. Jiang, Boosting photocatalytic hydrogen production of a metal-organic framework decorated with platinum nanoparticles: the platinum location matters, Angew. Chem. Int. Ed. 55 (32) (2016) 9389–9393.
[24] R. Kumar, D. Das, A.K. Singh, C_2N/WS_2 van der Waals type-II heterostructure as a promising water splitting photocatalyst, J. Catal. 359 (2018) 143–150.
[25] J.Y. Su1, S.J. Yu, M.Z. Xu, Y.X. Guo, X.B. Sun, Y.B. Fan, Z.Y. Zhang, J.F. Yan, W. Zhao, Enhanced visible light photocatalytic performances of few-layer MoS_2@TiO_2 hollow spheres heterostructures, Mater. Res. Bull. 130 (2020) 110936.
[26] Y.-P. Yuan, L.-W. Ruan, J. Barber, S.C. Joachim Loo, C. Xue, Hetero-nanostructured suspended photocatalysts for solar-to-fuel conversion, Energy Environ. Sci. 7 (12) (2014) 3934–3951.
[27] S.Q. Zhang, X. Liu, C.B. Liu, S.L. Luo, L.L. Wang, T. Cai, Y.X. Zeng, J.L. Yuan, W.Y. Dong, Y. Pei, Y.T. Liu, MoS_2 quantum dot growth induced by S vacancies in a $ZnIn_2S_4$ monolayer: atomic level heterostructure for photocatalytic hydrogen production, ACS Nano. 12 (2018) 751–758.
[28] Y. Kumar, R. Kumar, P. Raizada, A.A.P. Khan, Q.V. Le, P. Singh, V.H. Nguyen, Novel Z-scheme $ZnIn_2S_4$-based photocatalysts for solar-driven environmental and energy applications: progress and perspectives, J. Mater. Sci. Technol. 87 (2021) 234–325.
[29] J. Wang, S.J. Sun, R. Zhou, Y.Z. Li, Z.T. He, H. Ding, D.M. Chen, W.H. Ao, A review: synthesis, modification and photocatalytic applications of $ZnIn_2S_4$, J. Mater. Sci. Technol. 78 (2021) 1–19.
[30] Y. Pan, X.Z. Yuan, L.B. Jiang, H.B. Yu, J. Zhang, H. Wang, R.P. Guan, G.M. Zeng, Recent advances in synthesis, modification and photocatalytic applications of micro/nano-structured zinc indium sulfide, Chem. Eng. J. 354 (2018) 407–431.
[31] M. Wang, G. Zhang, Z. Guan, J. Yang, Q. Li, Spatially separating redox centers and photothermal effect synergistically boosting the photocatalytic hydrogen evolution of $ZnIn_2S_4$ nanosheets, Small 17 (17) (2021) 2006952.
[32] K.E. deKrafft, C. Wang, W. Lin, Metal-organic framework templated synthesis of Fe_2O_3/TiO_2 nanocomposite for hydrogen production, Adv. Mater. 24 (15) (2012) 2014–2018.
[33] F.Z. Song, W. Li, Y.J. Sun, Metal-organic frameworks and their derivatives for photocatalytic water splitting, Inorganics 5 (2017) 40.
[34] X.Q. Hao, Z.W. Cui, J. Zhou, Y.C. Wang, Y. Hu, Y. Wang, Z.G. Zou, Architecture of high efficient zinc vacancy mediated Z-scheme photocatalyst from metal-organic frameworks, Nano Energy 52 (2018) 105–116.
[35] H.-Y. Zhang, Y. Yang, C.-C. Li, H.-L. Tang, F.-M. Zhang, G.-L. Zhang, H. Yan, A new strategy for constructing covalently connected MOF@COF core-shell heterostructures for enhanced photocatalytic hydrogen evolution, J. Mater. Chem. A. 9 (31) (2021) 16743–16750.
[36] J.X. Xu, Y.H. Qi, C. Wang, L. Wang, NH_2-MIL-101(Fe)/Ni $(OH)_2$-derived C, N-codoped Fe_2P/Ni_2P cocatalyst modified g-C_3N_4 for enhanced photocatalytic hydrogen evolution from water splitting, Appl. Catal., B. 241 (2019) 178–186.
[37] Q.S. Zhang, Y.M. Li, H. Ren, Q.C. Zhai, C.L. Zhang, L. Cheng, Engineering full hollow and yolk-shell structures of Z-scheme photocatalysts for advanced hydrogen production, Chem. Eng. J. 408 (2021) 127267.
[38] X. Liu, L. Zhang, Y.D. Li, X.Z. Xu, Y.C. Du, Y.Q. Jiang, K.F. Lin, A novel heterostructure coupling MOF-derived fluffy porous indium oxide with g-C_3N_4 for enhanced photocatalytic activity, Mater. Res. Bull. 133 (2021) 111078.
[39] Y.X. Feng, T. Yan, T.T. Wu, N. Zhang, Q.Q. Yang, M. Sun, L.G. Yan, B. Du, Q. Wei, A label-free photoelectrochemical aptasensing platform base on plasmon Au coupling with MOF-derived In_2O_3@g-C_3N_4 nanoarchitectures for tetracycline detection, Sens. Actuat.: B. 298 (2019) 126817.
[40] J.-T. Ren, K. Yuan, K.e. Wu, L. Zhou, Y.-W. Zhang, A robust CdS/In_2O_3 hierarchical heterostructure derived from a metal-organic framework for efficient visible-light photocatalytic hydrogen, Prod. Inorg. Chem. Front. 6 (2) (2019) 366–375.
[41] L.M. Sun, Y. Zhuang, Y.S. Yuan, W.W. Zhan, X.J. Wang, X.G. Han, Y.L. Zhao, Nitrogen-doped carbon-coated CuO-In_2O_3 p-n heterojunction for remarkable photocatalytic hydrogen evolution, Adv. Energy Mater. 9 (2019) 1902839.
[42] Y.K. Sun, Q. Zhu, B. Bai, Y.L. Li, C. He, Novel all-solid-state Z-scheme SnO_2/Pt/In_2O_3 photocatalyst with boosted photocatalytic performance on water splitting and 2,4-dichlorophenol degradation under visible light, Chem. Eng. J. 390 (2020) 124518.
[43] H.L. Yang, J.Q. Tang, Y. Luo, X.Q. Zhan, Z. Liang, L. Jiang, H.L. Hou, W.Y. Yang, MOFs-derived fusiform In_2O_3 mesoporous nanorods anchored with ultrafine CdZnS nanoparticles for boosting visible-light photocatalytic hydrogen evolution, Small 17 (2021) 2102307.
[44] Q. Zhang, J. Zhang, X. Wang, L. Li, Y.-F. Li, W.-L. Dai, In-N-In sites boosting interfacial charge transfer in carbon coated hollow tubular In_2O_3/$ZnIn_2S_4$ heterostructure derived from In-MOF for enhanced photocatalytic hydrogen evolution, ACS Catal. 11 (10) (2021) 6276–6289.
[45] R. Sivasamy, F. Quero, K. Paredes-Gil, K.M. Batoo, M. Hadi, E.H. Raslam, Comparison of the electronic, optical and photocatalytic properties of $MoSe_2$, InN, and $MoSe_2$/InN heterostructure nanosheet – a first-principle study, Mater. Sci. Semicond. Process. 131 (2021) 105861.
[46] Z. Su, H. Li, P. Chen, S. Hu, Y. Yan, Novel heterostructured InN/TiO_2 submicron fibers designed for high performance visible-light-driven photocatalysis, Catal. Sci. Technol. 7 (21) (2017) 5105–5112.
[47] M. Dou, G. Baldissera, C. Persson, ZnO-InN nanostructures with tailored photocatalytic properties for overall water-splitting, Int. J. Hydrogen Energy. 38 (36) (2013) 16727–16732.
[48] X. Hou, S. Jiang, Y. Li, J. Xiao, Y. Li, Ni-doped InN/GaZnON composite catalyst for overall water splitting under visible light irradiation, Int. J. Hydrogen Energy. 40 (45) (2015) 15448–15453.
[49] G. Kresse, J. Furthmüller, Efficient iterative schemes for ab initio total-energy calculations using a plane-wave basis set, Phys. Rev. B. 54 (16) (1996) 11169–11186.
[50] J.P. Perdew, K. Burke, M. Ernzerhof, Generalized gradient approximation made simple, Phys. Rev. Lett. 77 (18) (1996) 3865–3868.
[51] G. Kresse, D. Joubert, From ultrasoft pseudopotentials to the projector augmented-wave method, Phys. Rev. B. 59 (3) (1999) 1758–1775.
[52] P.E. Blöchl, Projector augmented-wave method, Phys. Rev. B. 50 (24) (1994) 17953–17979.
[53] S. Grimme, J. Antony, S. Ehrlich, H. Krieg, A consistent and accurate ab initio parametrization of density functional dispersion correction (DFT-D) for the 94 elements H-Pu, J. Chem. Phys. 132 (2010) 154104.
[54] G. Henkelman, B.P. Uberuaga, H. Jonsson, A climbing image nudge elastic band method for finding saddle points and minimum energy paths, J. Chem. Phys. 113 (2000) 9901–9904.
[55] C.J. Xie, X.Y. Lu, F. Deng, X.B. Luo, J. Gao, D.D. Dionysiou, Unique surface structure of nano-sized $CuInS_2$ anchored on rGO thin film and its superior photocatalytic activity in real wastewater treatment, Chem. Eng. J. 338 (2018) 591–598.
[56] A. Reheman, Y. Tursun, T. Dilinuer, M. Halidan, K. Kadeer, A. Abulizi, Facile one-step sonochemical synthesis and photocatalytic properties of graphene/Ag_3PO_4 quantum dots composites, Nanoscale Res. Lett. 13 (2018) 70.
[57] Y.J. Chen, H. Ge, L. Wei, Z.H. Li, R.S. Yuan, P. Liu, X.Z. Fu, Reduction degree of reduced graphene oxide (RGO) dependence of photocatalytic hydrogen evolution performance over RGO/$ZnIn_2S_4$ nanocomposites, Catal. Sci. Technol. 3 (2013) 1712–1717.
[58] H.J. Yu, R. Shi, Y.X. Zhao, T. Bian, Y.F. Zhao, C. Zhou, G.I.N. Waterhouse, L.Z. Wu, C.H. Tung, T.R. Zhang, Alkali-assisted synthesis of nitrogen deficient graphitic carbon nitride with tunable band structures for efficient visible-light-driven hydrogen evolution, Adv. Mater. 29 (2017) 1605148.